Linkage Between Micro- and Nano-Raman Spectroscopy of Defects in Graphene

Cassiano Rabelo[1,2] Thiago L. Vasconcelos,[3] Bruno C. Publio,[2] Hudson Miranda[1]
Luiz Gustavo Cançado,[2] and Ado Jorio[1,2,*]

[1]*Graduate Program in Electrical Engineering – UFMG – CEP: 31270-901, Belo Horizonte, Minas Gerais, Brazil*
[2]*Departamento de Física – UFMG – CEP: 31270-901, Belo Horizonte, Minas Gerais, Brazil*
[3]*Divisão de Metrologia de Materiais – Inmetro – CEP: 25250-020, Duque de Caxias, Rio de Janeiro, Brazil*

On nanomaterials characterization, the evolution from the broadly utilized micro-Raman spectroscopy to a nanoscale regime is taking place with the improvements in tip-enhanced Raman spectroscopy (TERS). It is not clear, however, to which extent protocols developed within the diffraction-limited far-field configuration apply to the near-field regime. Defects in graphene nanoflakes are investigated in this work in both micro and nano regimes, showing that the Raman characteristics utilized to quantify defects in the far-field regime actually change in the presence of the TERS tip, generating incompatible results. The micro-to-nano spectral mismatch can be modeled using a theory of spatial coherence in near-field Raman scattering, from which a parameterization procedure can be derived in order to obtain consistent results. The incompatibilities observed here for graphene should also happen in other structures relevant to nanoscience and nanotechnology when explored in the nano-Raman regime, and they can be resolved similarly.

I. INTRODUCTION

Owing to outstanding resolution to probe materials' energy levels, which can reach 1 μeV, Raman spectroscopy is a technique that enables identifying, qualifying, and quantifying material properties accurately. For instance, defects, which can modify the physicochemical properties of crystalline lattices, have been broadly studied using this light scattering technique, in different classes of materials [1–9], including low-dimensional nanostructures (zero [3,4], one [5,10], and two dimensional [6–8,10]). However, being an optical phenomenon, micro-Raman spectroscopy is resolution limited by diffraction, as formalized by the Rayleigh criterion [11], where features smaller than hundreds of nanometers, or approximately half of the wavelength of the excitation light source, cannot be spatially resolved, therefore hindering its application in nanotechnology.

The spatial resolution limit has been overcome with the development of tip-enhanced Raman spectroscopy (TERS) [12–17], in which a metallic tip works as a nanoantenna, converting light into localized near-field energy and vice versa [18]. In TERS the spatial resolution is no longer limited by the wavelength of the incident light, but it is defined by the tip's apex, which is typically in the order of tens of nanometers in diameter. Under very special conditions, TERS can even reach subnanometer resolution [19,20]. As

such, TERS allows for the observation of a single doping atom in the wall of a carbon nanotube [21], showing that Raman spectroscopy can no longer be considered a diffraction limited analytical tool, but it entered the nano realm.

It remains to be demonstrated, however, whether TERS can be utilized to probe surface properties that are hidden in the micron-sized confocal background of optical microscopy, especially problematic in two-dimensional systems, like graphene [16]. The success of the technique depends on plasmonic tips capable of generating a local (nanometer) signal that overcomes the response from the micron-sized illumination area in a two-dimensional system [14,17,18]. Here we show that a plasmon-tunable tip pyramid (PTTP) stripped out of a silicon patterned template wafer [22] is capable of generating high enough nano-Raman signals to provide nearly background-free local information on graphene, without using extra enhancement from metallic substrates (gap mode) or any pre or postsignal processing. In doing so, our results show relevant inconsistencies between micro- and nano-Raman results that can be understood based on interference effects that play a role only in the near-field TERS configuration [23]. These interference effects can be either constructive or destructive depending on the symmetry of the phonon giving rise to a specific Raman signal, therefore generating more or less signal enhancements for different phonon modes, with the relative enhancement also depending on the phonon coherence length [23–26]. This effect

---

*adojorio@fisica.ufmg.br

has already been demonstrated when comparing the TERS signal from two Raman-allowed bands in graphene (the so-called *G* and 2*D* bands [24]) and it will play a role in the observations reported here.

In the following, we introduce the technical details (Sec. II), followed by the experimental results and discussions (Sec. III) and the concluding remarks (Sec. IV).

II. TECHNICAL DETAILS

The TERS system utilized here for nano-Raman measurements works on a backscattering configuration using a Nikon inverted microscope, equipped with a 60 times oil immersion objective (1.4 numerical aperture), as described in Ref. [27]. In this configuration, light comes from the bottom, and the incident light from a radially polarized helium-neon laser (632.8 nm wavelength) crosses a transparent substrate (a glass coverslip) to reach the graphene sample and the TERS tip, which is held in position from the top using a tuning fork–based home-built atomic force microscopy scan head. To acquire the backscattered Raman spectra, we use an Andor Shamrock SR-303i spectrometer equipped with an iDus DU401A-BR-DD charge coupled device. The Raman scattered signal is dispersed by a 600 lines/mm grating, resulting in a spectral resolution of approximately 2.36 cm^{-1}, as experimentally determined. Five physically different gold PTTPs are utilized in the experimental procedures, with tip apex diameters $d = (30 \pm 10)$ nm and sizes chosen to tune the localized surface plasmon resonance with the helium-neon laser [22], as determined by scanning electron microscopy. For micro-Raman measurements, the TERS tip is simply retracted and kept at a distance of at least 700 nm away from the sample surface.

Spectra from pristine single-layer graphene comes from a sample prepared by mechanical exfoliation of a highly pure and ordered natural graphite. The samples of graphene nanoflakes are based on commercially available graphene powders, from FGV Cambridge Nanosystems Ltd., under the name CamGraph G1 graphene powder. According to the manufacturer, the powder consists of graphene flakes with one to five layers, derived from a catalyst and surfactant-free microwave plasma synthesis process. The samples are all deposited on a glass coverslip for the measurements.

III. RESULTS AND DISCUSSION

In Figs. 1(a) and 1(b) we show the Raman spectra from a crystalline single-layer graphene and from a defective graphene nanoflake, respectively, while in Figs. 1(c) and 1(d) we show these samples as spectrally imaged. The red and green spectra in Figs. 1(a) and 1(b) are measured with and without the presence of the TERS tip, in the region encompassing the disorder-induced *D* band (approximately 1350 cm^{-1}), the pristine first-order

Raman-allowed *G* band (approximately 1584 cm^{-1}), and the second-order Raman-allowed 2*D* band (approximately 2700 cm^{-1}, also called *G′* in the literature). The TERS near-field (NF) intensities from the two-dimensional crystalline graphene [Fig. 1(a)] is roughly 20 times larger than the confocal far-field (FF) signals (19 times larger for the *G* band and 26 times larger for the 2*D* band). These results are remarkable because the NF signal comes from an area two orders of magnitude smaller than that of the FF signal [see the inset to Fig. 1(a)], so that the actual local field enhancement [28] achieved in this experiment is in the order of 10^3. Spectral enhancements of that order have been observed in highly localized structures, i.e., when TERS enhances the signal from where the emitter is located and it does not compete with the far-field background signal [21], different from the present case, where the graphene sample covers the entire confocal region [Fig. 1(a)]. For the nanoflake, the Raman signal is not even observable in the absence of the tip, as shown by the green spectrum in Fig. 1(b), taken with the TERS tip away from the sample. Because the Raman spectrum obtained in the presence of the tip is comprised of both the FF and NF signals together, from now on we refer to spectra acquired without and with the presence of the TERS tip as micro-Raman (μR) and nano-Raman (nR) spectra, respectively.

Micro-Raman and nano-Raman spectroscopy has been performed on distinct defective graphene nanoflakes, using different PTTPs. In Fig. 2 we present results obtained from four samples, one per row. The first column [Fig. 2(a)] shows the images generated based on the spectral range of the graphene's *D* band, as extracted from the μR hyperspectral intensity, while the second column [Fig. 2(b)] shows the images generated based on the same spectral range as Fig. 2(a), but extracted from the nR hyperspectral intensity, which is consistent with the atomic force microscopy (AFM) topography image [Fig. 2(c)] acquired simultaneously during the optical scan procedure. Note in Fig. 2(b) the coexistence of the NF (sharp-edged structures, coincident with topography images) and FF (blurred structures, coincident with μR images) signals. Because of the differences in tip enhancement, which directly influence the NF over FF image contrast, flake *A* in Fig. 2 is fully dominated by the NF signal, while flake *D* has a strong FF contribution.

The fourth column [Fig. 2(d)] shows the spectral crystalline-order figure of merit, which is the A_D/A_G histogram for each nanoflake, where A_D and A_G are the integrated intensities (areas) of the *D* and *G* bands, respectively. The μR (green) and nR (red) data are shown on the same plot. It is important to note that the spectrally weighted mean values for the μR and nR distributions, represented in Fig. 2(d) by the green and red crosses, respectively, at the *x* axis, do not coincide. Flake *A* shows the largest deviation, whereas flake *D* shows the smallest deviation. In order to compare these deviations, in

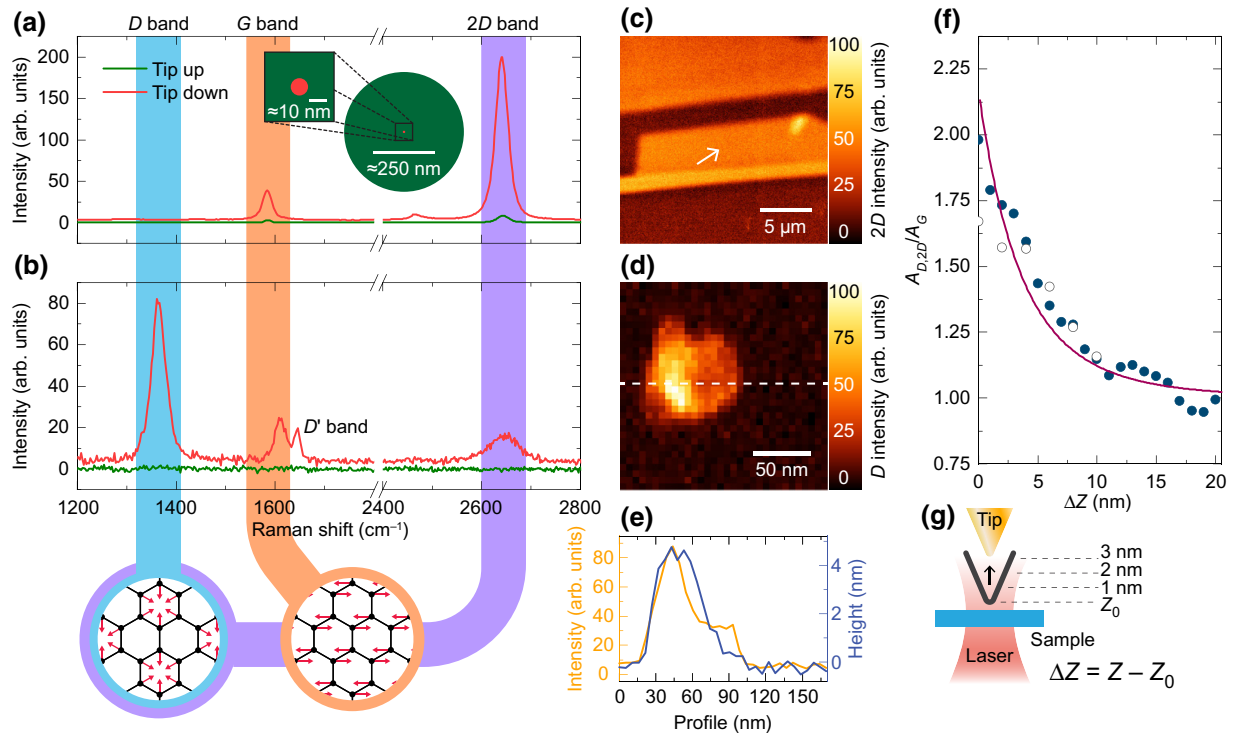FIG. 1. (a) Micro-Raman (μR, green line) and nano-Raman (nR, red line) spectra of pristine single-layer graphene. The inset schematically shows the areas from where the μR and nR spectra come from in relation to each other. (b) Raman spectra from a defective graphene nanoflake, as can be inferred from the presence of the D band, highlighted in blue. The spectra are acquired without (μR, green line) and with (nR, red line) the presence of the TERS tip. The D' band (approximately 1610 cm^{-1}), which, as the D band is associated with disorder, is also visible. The G and $2D$ bands are highlighted in orange and purple, respectively. Inside the circles are the associated eigenvectors. (c) The μR $2D$-band intensity image of the pristine graphene. The white arrow indicates where the Raman data in (a) were taken. (d) The nR D-band image of the graphene nanoflake from where the data in (b) were taken. The topography (atomic force microscopy) and D-band intensity line profile along the white dashed line are shown in (e) with blue and orange lines, respectively. (f) Plot of the area ratio between the $2D$ and G (A_{2D}/A_G, filled circles) bands of pristine graphene [panels (a),(c)] and between the D and G (A_D/A_G, open circles) bands of the nanoflake [panels (b),(d)] for different tip-sample distances ΔZ [see (g)]. Note that, although the tip-approach procedure performed on the nanoflake retracted the tip as far as $\Delta Z = 20$ nm, the acquired spectra only exhibited a signal-to-noise ratio significant enough to be fitted up to $\Delta Z = 10$ nm. The red line represents the theoretical fit (see the text).

Fig. 2(e) we show a scatter plot of the nR/$\bar{\mu}$R normalized $(A_D/A_G)^*$ as a function of A_D^* for the four flakes, where the asterisk indicates that the nR data is normalized by the average value of the μR data ($\bar{\mu}$R), i.e., $(A_D/A_G)^* = [(A_D/A_G)^{\mathrm{nR}}/(\bar{A}_D/\bar{A}_G)^{\mu\mathrm{R}}]$ and $A_D^* = [(A_D)^{\mathrm{nR}}/(\bar{A}_D)^{\mu\mathrm{R}}]$. The reason for choosing the area of the D band for the x axis is because it provides a metric for the spectral enhancement obtained at each nR spectrum. There is a clear trend in Fig. 2(e), with the data obtained from flake A concentrated in the upper-right part of the graph, and the data obtained from flake D concentrated in the lower-left part of the graph. The data spread for each specific flake reflects sample inhomogeneity. It is relevant to observe that these results contradict the assumed expectation where the normalized average of all spectra from the spatially resolved NF and the unresolved FF should yield similar

results defined by the sample, not by the experimental procedure.

What we call here "the assumed expectation" for coincident mean A_D/A_G distributions on nR and μR regimes comes from the consideration that Raman scattering is a spatially incoherent process, without considering that in the near-field regime, field coherence must be taken into account, and the resulting interference effect depends on the symmetry of the vibrational mode, as already established for graphene [23–25] and GaS [26]. This is clearly shown by the filled circles in Fig. 1(f), which show the changes in the A_{2D}/A_G ratio between the integrated areas of the Raman-allowed $2D$ and G bands obtained from a pristine graphene sample, when changing the distance between the tip and the sample ΔZ [as depicted in Fig. 1(g)]. The data is normalized by the area of each
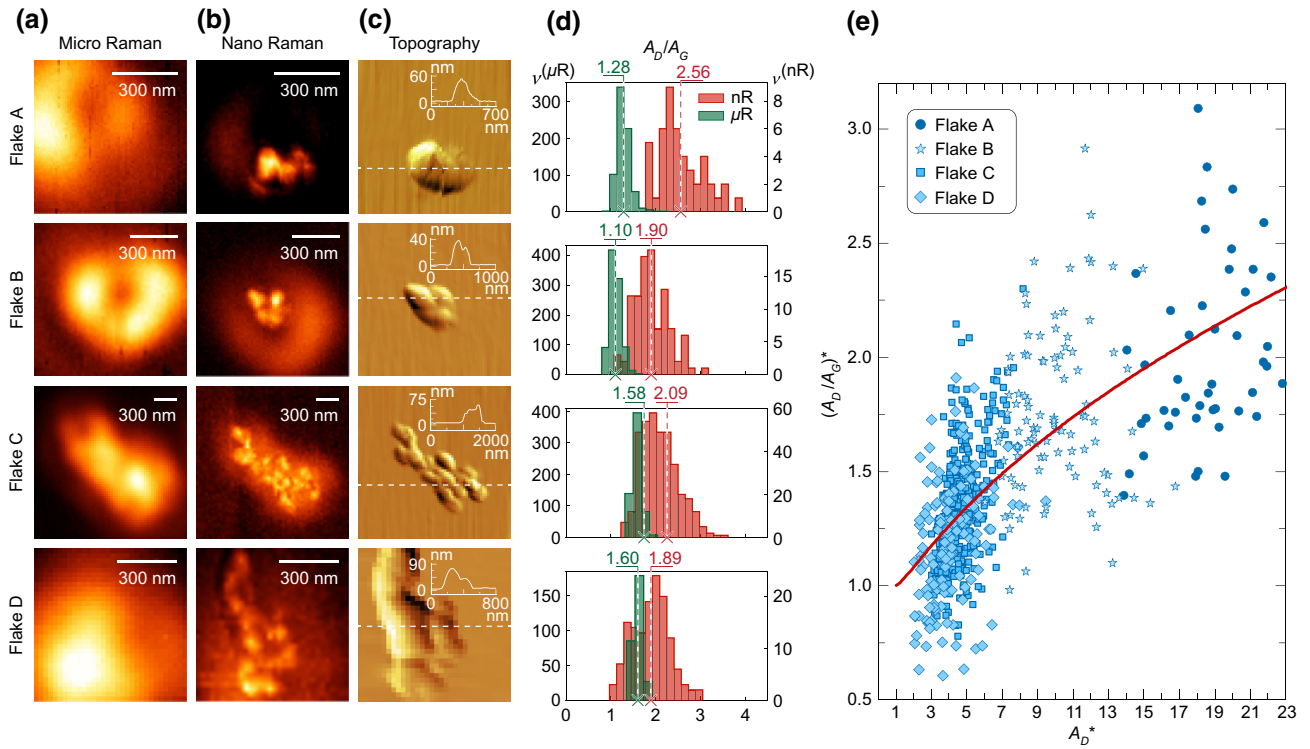
FIG. 2. Nanoflake micro-Raman versus nano-Raman analysis. The first (a) and second (b) columns show images generated from the μR and nR hyperspectral Raman data, respectively, acquired based on the intensity of the D band. The scan area is the same for both μR and nR. The third column (c) is the AFM topography image acquired during the TERS (nR) scan. The insets are line profiles obtained along the white dashed lines. The fourth column (d) shows histograms of the (A_D/A_G) ratio for both μR (green) and nR (red) acquired spectra, while the green and red crosses represent the spectrally weighted mean values for the μR and n distributions, respectively. In (a)–(d) each line displays the analysis from one distinct nanoflake. (e) Scatter plot of the nR/$\bar{\mu}$R normalized values $(A_D/A_G)^*$ as a function of A_D^* for the nanoflakes investigated. The red line represents the theoretical fit of the data points using Eq. (1). All the nanoflake measurements are performed using 1 s of accumulation time per pixel. The μR and nR results are obtained with 4.8 and 0.45 mW excitation powers at the sample, respectively. The hyperspectra are composed of 64×64 pixels, except for flake D, which is composed of 32×32 pixels.

respective band at the far-field configuration ($\Delta Z = 20$ nm), while $\Delta Z = 0$ corresponds to the tip interacting with the sample, commonly considered to be $Z_0 \approx 5$ nm [13]. As shown, with the presence of the tip at $\Delta Z = 0$, the enhancement of the 2D band is approximately twice the enhancement exhibited by the G band, with this difference decreasing as ΔZ increases.

Although the D and 2D bands originate from different scattering processes, the first being defect activated, while the second is a second-order Raman allowed process, they are related to the same phonons in the interior of the graphene Brillouin zone, nearly totally symmetric (A_{1g}) [25]. Therefore, the D band is expected to exhibit the same near-field interference properties as the 2D band. In Fig. 1(f) we also exhibit the A_D/A_G data (open circles) from the tip-approach procedure conducted in the graphene nanoflake shown in Figs. 1(b) and 1(d), with the last point ($\Delta Z = 10$ nm) normalized to the pristine 2D data (filled circles).

The solid red curve in Fig. 1(f) represents the theoretical fit considering spatially coherent Raman scattering [23]. Therefore, the near-field interference effects for the modes with different symmetries (E_{2g} for the G band and A_{1g} for the D and 2D bands) are the reason why the mean (A_D/A_G) values for the nR (red crosses) and μR (green crosses) distributions in Fig. 2(d) do not coincide.

Differently from Fig. 1(f), where the TERS enhancement is changed by changing ΔZ, in Fig. 2(e) ΔZ is fixed at $\Delta Z = 0$ ($Z = Z_0$), and the change in the TERS enhancement is measured by the D-band spectral enhancement. In this case, the theoretically expected trend for the nR/$\bar{\mu}$R normalized $(A_D/A_G)^*$ versus A_D^* data is given by the red line in Fig. 2(e) [23].

Although modeling with the theory of spatial coherence in near-field Raman scattering requires costly numerical integration over the two-dimensional sample space [23], the basic ingredients can be rationalized, and they are summarized in Fig. 3. Depending on the symmetry of the
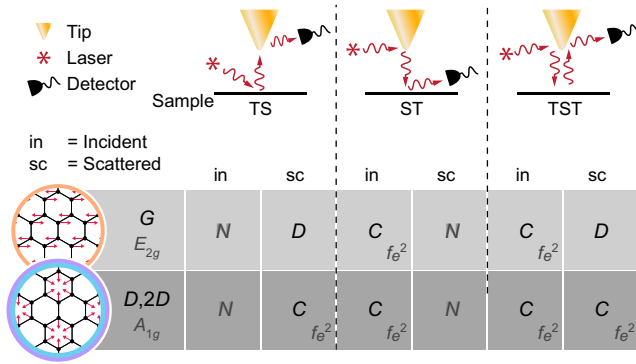
FIG. 3. Classification of interference effects in the TERS signal from graphene. Top row: Illustration of sequences of field-sample (S) and field-tip (T) interactions. The TS series represents the incident field interacting with the sample, followed by the scattered field interacting with the tip; ST represents the incident field interacting with the tip and then with the sample; in TST, the incident field interacts first with the tip and then with the sample, and the scattered field finally interacts with the tip. Middle row: The G mode (E_{2g}) presents constructive interference (marked with the C character) when the incident field reaches the tip in the ST and TST events. Bottom row: For the D and $2D$ modes (A_{1g}), the constructive interactions occur for the scattered field in TS, for the incident field in ST, and for both the incident and scattered fields in the TST sequence. Each constructive event enhances the signal strength by f_e^2, as indicated. Events that generate destructive interference are marked with D, while N indicates no interference.

associated vibrational mode and on the sequence of scattering events caused by interactions of incident and scattered fields with the sample (S) and tip (T), the interference can be either destructive (D) or constructive (C) [23]. Field interference (D or C) occurs only for light (incident or scattered) interacting with the tip, with no interference (N) occurring when light interacts with the sample. The relevant interactions are illustrated in the upper row of Fig. 3.

The G mode (E_{2g} symmetry) presents constructive (C) interference only when the incident field reaches the tip (T) in the ST and TST events. For the D and $2D$ modes (A_{1g} symmetry), constructive (C) interactions occur for the scattered field in TS, for the incident field in ST, and for both the incident and scattered fields in the TST sequence. Therefore, considering that the nR intensities depend on the field enhancement factor f_e, so that each constructive event enhances the signal strength by f_e^2 [23], the integrated intensities (areas) of the graphene bands exhibit the dependencies $A_G^{nR} = A_G^{FF} + A_G^{NF} = A_G^{\mu R}(1 + c_1 f_e^2)$ and $A_D^{nR} = A_D^{FF} + A_D^{NF} = A_D^{\mu R}(1 + c_2 f_e^2 + c_3 f_e^4)$, respectively. Isolating f_e in these equations leads to a simple formula that can be used to describe the evolution of the interference

effect on $(A_D/A_G)^{nR}$:

$$\left(\frac{A_D}{A_G}\right)^* = \frac{A_D^*}{1 + \alpha[\sqrt{1 - \beta(1 - A_D^*)} - 1]}. \quad (1)$$

Here $\alpha = c_1 c_2/2c_3$ and $\beta = 4c_3/c_2^2$ measure the weights of the quadratic and fourth-power terms of f_e to the nR peak intensities. The red line in Fig. 2(e) represents the fit to the experimental data through Eq. (1), giving $\alpha = (3.33 \pm 0.39)$ and $\beta = (0.58 \pm 0.09)$.

IV. CONCLUSION

In conclusion, for a given TERS spectral enhancement in graphene, the red line in Fig. 2(e) [or, equivalently, Eq. (1)] has to be used to parameterize the nano-Raman $(A_D/A_G)^{nR}$ observed value, so that the nR and μR mean (A_D/A_G) values, as observed in the histograms of Fig. 2, coincide. In this way, the connection between μR and nR is established, i.e., nR can make use of the μR protocols established in the literature [10,29–32] for defect quantification in graphene related materials.

The physics summarized in Fig. 3 is not limited to the D and G bands in graphene, it applies directly to any A_{1g} and E_{2g} symmetry phonons. Similar reasoning can also be developed to other phonon symmetries, and even to phonons with the same symmetry but different phonon coherence lengths. These statements consider spatial coherence effects like observed in the defect-induced band in graphene [30], but further work may be needed to parameterize the nR protocols for other sp^2 carbon [8–10,29,33,34] and non-sp^2 carbon nanostructures [3–7], thus generating information that does not come easily with other microscopy techniques, especially in such a noninvasive way, relevant to nanoscience, nanometrology, and industry-related processes.

[1] D. W. Feldman, M. Ashkin, and J. H. Parker, Raman Scattering by Local Modes in Germanium-Rich Silicon-Germanium Alloys, Phys. Rev. Lett. **17**, 1209 (1966).

[2] N. Theodorakopoulos and J. Jäckle, Low-frequency Raman scattering by defects in glasses, Phys. Rev. B **14**, 2637 (1976).

[3] S. Prawer, K. Nugent, D. Jamieson, J. Orwa, L. Bursill, and J. Peng, The Raman spectrum of nanocrystalline diamond, Chem. Phys. Lett. **332,** 93 (2000).

[4] M. Šćepanović, M. Grujić-Brojčin, K. Vojisavljević, S. Bernik, and T. Srećković, Raman study of structural disorder in ZnO nanopowders, J. Raman Spectrosc. **41,** 914 (2010).

[5] B. Li, D. Yu, and S.-L. Zhang, Raman spectral study of silicon nanowires, Phys. Rev. B **59,** 1645 (1999).

[6] S. Mignuzzi, A. J. Pollard, N. Bonini, B. Brennan, I. S. Gilmore, M. A. Pimenta, D. Richards, and D. Roy, Effect of disorder on Raman scattering of single-layer MoS2, Phys. Rev. B **91,** 195411 (2015).

[7] J. Pei, X. Gai, J. Yang, X. Wang, Z. Yu, D.-Y. Choi, B. Luther-Davies, and Y. Lu, Producing air-stable monolayers of phosphorene and their defect engineering, Nat. Commun. **7,** 10450 (2016).

[8] Y. Cao, V. Fatemi, S. Fang, K. Watanabe, T. Taniguchi, E. Kaxiras, and P. Jarillo-Herrero, Unconventional superconductivity in magic-angle graphene superlattices, Nature **556,** 43 (2018).

[9] M. S. Dresselhaus and R. Kalish, *Ion Implantation in Diamond, Graphite and Related Materials*, Springer Series in Materials Science Vol. 22 (Springer Berlin Heidelberg, Berlin, Heidelberg, 1992).

[10] M. S. Dresselhaus, A. Jorio, M. Hofmann, G. Dresselhaus, and R. Saito, Perspectives on carbon nanotubes and graphene Raman spectroscopy, Nano Lett. **10,** 751 (2010).

[11] L. Rayleigh, Investigations in optics, with special reference to the spectroscope, The London, Edinburgh, Dublin Philos. Mag. J. Sci. **8,** 261 (1879).

[12] R. M. Stöckle, Y. D. Suh, V. Deckert, and R. Zenobi, Nanoscale chemical analysis by tip-enhanced Raman spectroscopy, Chem. Phys. Lett. **318,** 131 (2000).

[13] L. Novotny and B. Hecht, *Principles of Nano-Optics* (Cambridge University Press, Cambridge, 2012).

[14] B. Pettinger, P. Schambach, C. J. Villagómez, and N. Scott, Tip-enhanced Raman spectroscopy: Near-fields acting on a few molecules, Annu. Rev. Phys. Chem. **63,** 379 (2012).

[15] T. Deckert-Gaudig, A. Taguchi, S. Kawata, and V. Deckert, Tip-enhanced Raman spectroscopy-from early developments to recent advances, Chem. Soc. Rev. **46,** 4077 (2017).

[16] F. Shao and R. Zenobi, Tip-enhanced Raman spectroscopy: Principles, practice, and applications to nanospectroscopic imaging of 2D materials, Anal. Bioanal. Chem. **411,** 37 (2019).

[17] N. Kumar, B. M. Weckhuysen, A. J. Wain, and A. J. Pollard, Nanoscale chemical imaging using tip-enhanced Raman spectroscopy, Nat. Protoc. **14,** 1169 (2019).

[18] L. Novotny and N. van Hulst, Antennas for light, Nat. Photonics **5,** 83 (2011).

[19] R. Zhang, Y. Zhang, Z. C. Dong, S. Jiang, C. Zhang, L. G. Chen, L. Zhang, Y. Liao, J. Aizpurua, Y. Luo, J. L. Yang, and J. G. Hou, Chemical mapping of a single molecule by plasmon-enhanced Raman scattering, Nature **498,** 82 (2013).

[20] J. Lee, K. T. Crampton, N. Tallarida, and V. A. Apkarian, Visualizing vibrational normal modes of a single molecule with atomically confined light, Nature **568,** 78 (2019).

[21] I. O. Maciel, N. Anderson, M. A. Pimenta, A. Hartschuh, H. Qian, M. Terrones, H. Terrones, J. Campos-Delgado, A. M. Rao, L. Novotny, and A. Jorio, Electron and phonon renormalization near charged defects in carbon nanotubes, Nat. Mater. **7,** 878 (2008).

[22] T. L. Vasconcelos, B. S. Archanjo, B. S. Oliveira, R. Valaski, R. C. Cordeiro, H. G. Medeiros, C. Rabelo, A. Ribeiro, P. Ercius, C. A. Achete, A. Jorio, and L. G. Cançado, Plasmon-tunable tip pyramids: Monopole nanoantennas for near-field scanning optical microscopy, Adv. Opt. Mater. **6,** 1800528 (2018).

[23] L. G. Cançado, R. Beams, A. Jorio, and L. Novotny, Theory of Spatial Coherence in Near-Field Raman Scattering, Phys. Rev. X **4,** 031054 (2014).

[24] R. Beams, L. G. Cançado, S.-H. Oh, A. Jorio, and L. Novotny, Spatial Coherence in Near-Field Raman Scattering, Phys. Rev. Lett. **113,** 186101 (2014).

[25] A. Jorio, N. S. Mueller, and S. Reich, Symmetry-derived selection rules for plasmon-enhanced Raman scattering, Phys. Rev. B **95,** 155409 (2017).

[26] R. S. Alencar, C. Rabelo, H. L. S. Miranda, T. L. Vasconcelos, B. S. Oliveira, A. Ribeiro, B. C. Públio, J. Ribeiro-Soares, A. G. S. Filho, L. G. Cançado, and A. Jorio, Probing spatial phonon correlation length in post-transition metal monochalcogenide gaS using tip-enhanced Raman spectroscopy, Nano Lett. **19,** 7357 (2019).

[27] C. Rabelo, H. Miranda, T. L. Vasconcelos, L. G. Cancado, and A. Jorio, in *2019 4th International Symposium on Instrumentation Systems, Circuits and Transducers (INSCIT)* (IEEE, São Paulo, 2019), p. 1.

[28] T. L. Vasconcelos, B. S. Archanjo, B. S. Oliveira, W. F. Silva, R. S. Alencar, C. Rabelo, C. A. Achete, A. Jorio, and L. G. Cancado, Optical nanoantennas for tip-enhanced Raman spectroscopy, IEEE J. Sel. Top. Quantum Electron. **00,** 1 (2020).

[29] A. C. Ferrari and D. M. Basko, Raman spectroscopy as a versatile tool for studying the properties of graphene, Nat. Nanotechnol. **8,** 235 (2013).

[30] M. Lucchese, F. Stavale, E. M. Ferreira, C. Vilani, M. Moutinho, R. B. Capaz, C. Achete, and A. Jorio, Quantifying ion-induced defects and Raman relaxation length in graphene, Carbon **48,** 1592 (2010).

[31] L. G. Cançado, A. Jorio, E. H. M. Ferreira, F. Stavale, C. A. Achete, R. B. Capaz, M. V. O. Moutinho, A. Lombardo, T. S. Kulmala, and A. C. Ferrari, Quantifying defects in graphene via Raman spectroscopy at different excitation energies, Nano Lett. **11,** 3190 (2011).

[32] L. Gustavo Cançado, M. Gomes da Silva, E. H. Martins Ferreira, F. Hof, K. Kampioti, K. Huang, A. Pénicaud, C. Alberto Achete, R. B. Capaz, and A. Jorio, Disentangling contributions of point and line defects in the Raman spectra of graphene-related materials, 2D Mater. **4,** 025039 (2017).

[33] M. A. Pimenta, G. Dresselhaus, M. S. Dresselhaus, L. G. Cançado, A. Jorio, and R. Saito, Studying disorder in graphite-based systems by Raman spectroscopy, Phys. Chem. Chem. Phys. **9,** 1276 (2007).

[34] A. C. Ferrari and J. Robertson, Interpretation of Raman spectra of disordered and amorphous carbon, Phys. Rev. B **61,** 14095 (2000).